

Nonequilibrium Thermodynamics of Hydrate Growth on a Gas-Liquid Interface

Xiaojing Fu,¹ Luis Cueto-Felgueroso,^{1,2} and Ruben Juanes^{1,*}¹Massachusetts Institute of Technology, 77 Massachusetts Avenue, Building 1, Cambridge, Massachusetts 02139, USA²Technical University of Madrid, Calle del Profesor Aranguren 3, 28040 Madrid, Spain

(Received 28 September 2017; revised manuscript received 16 January 2018; published 2 April 2018)

We develop a continuum-scale phase-field model to study gas-liquid-hydrate systems far from thermodynamic equilibrium. We design a Gibbs free energy functional for methane-water mixtures that recovers the isobaric temperature-composition phase diagram under thermodynamic equilibrium conditions. The proposed free energy is incorporated into a phase-field model to study the dynamics of hydrate formation on a gas-liquid interface. We elucidate the role of initial aqueous concentration in determining the direction of hydrate growth at the interface, in agreement with experimental observations. Our model also reveals two stages of hydrate growth at an interface—controlled by a crossover in how methane is supplied from the gas and liquid phases—which could explain the persistence of gas conduits in hydrate-bearing sediments and other nonequilibrium phenomena commonly observed in natural methane hydrate systems.

DOI: 10.1103/PhysRevLett.120.144501

The main point is clear in the abstract.

The abstract is succinct and direct

Background

Methane hydrate is an icelike solid that forms out of an aqueous solution of water and dissolved methane under moderate pressure and low temperature conditions [1] [Fig. 1(a)]. A large body of work over the past few decades has established a fundamental understanding of methane hydrate thermodynamics [2]. Combining experimental data with free-energy-minimization techniques, current simulators are able to accurately predict the equilibrium phase diagram of the water-methane system [e.g., Fig. 1(b)] under a wide range of pressure, temperature, and compositional conditions [3–6]. Nonequilibrium thermodynamic conditions, however, may persist for long times in natural hydrate systems, and need to be better understood. For instance, the equilibrium phase diagram predicts that, under hydrate-forming temperature, two-phase coexistence of hydrate with either methane gas or aqueous solution is energetically favored; three-phase coexistence with gas, liquid, and hydrate is only permitted at the triple-point temperature and pressure. In reality, such three-phase coexistence has been observed at many different spatial and temporal scales where the triple-point conditions are not satisfied. At the field scale, *in situ* surveys reveal that gas pockets can coexist with hydrate and water within marine sediments for a long period of time [7–9]. At the millimeter scale, both field studies [10–15] and controlled laboratory experiments [16–19] have shown that a layer of hydrate shell can survive on a gas bubble in water column for extended periods of time. At the micrometer scale, pockets of oversaturated metastable water can coexist with hydrate when formed in the presence of gas bubbles [20].

These nonequilibrium states have long been attributed to a diffusion-limited kinetic effect [21]. However, at the heart of these phenomena is the challenge to understand a rather

Research question

simple problem: how does hydrate grow on the interface between a hydrocarbon or gas phase and the ambient water phase? Experimental studies have focused on the direction and rate of growth on a macroscopic scale [17,22], the influence of subcooling and aqueous composition on growth rate [23–25], and the micron-scale details of the growth process [20,26,27]. Numerical studies have focused on developing parametrized kinetic growth models [28,29]. What is missing is an integrated modeling framework that can incorporate consistent hydrate thermodynamics into descriptions of multiphase mixtures, and provide mechanistic understanding of the nonequilibrium thermodynamic control of hydrate growth on a macroscopic gas-liquid interface. Such a model would help address important questions of hydrate formation in a multiphase environment, including seafloor crater formation by hydrate-controlled gas expulsion [30], the fate of hydrate-crusting bubbles ascending in the water column [15,19,31], and the

Knowledge gap

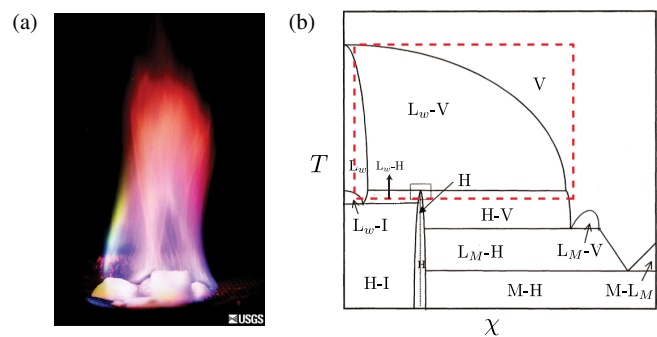


FIG. 1. (a) Burning of solid (white) methane hydrate (source: USGS). (b) Isobaric methane-water T - χ phase diagram adapted from [5,6].

stability of hydrate within seafloor sediments under a changing climate [32].

Phase-field modeling is a mathematical framework well suited to describe systems out of thermodynamic equilibrium [33,34]. First introduced in the context of solidification and phase transitions [35], it has since been adopted in the field of multiphase flow [36–46]. The phase-field approach is built upon a mathematical description of the free energy of the system. A phase variable, denoted $\phi_\alpha \in [0, 1]$, is chosen to represent the volume fraction of the phase α at any given point in the domain. Under this framework, the fluid interface is naturally described as a diffuse profile of ϕ_α , a feature that facilitates thermodynamic consistency with the physical system, and leads to robust computational schemes [47,48].

In classical thermodynamics simulators, the process of constructing phase diagrams based on energy descriptions is often referred to as Gibbs free energy minimization, where the equilibrium states along with some undetermined parameters are solved for through an iterative optimization procedure, constrained by experimental measurements [3,49,50]. A convenient approach to thermodynamic modeling in the phase-field framework is to derive the Gibbs free energy of multiphase, multicomponent mixtures by blending individual phase free energies. This idea has been adopted in many phase-field models, in the context of alloy solidification [51], liquid phase separation [52], and hydrate formation in an aqueous solution (not on an interface) [53,54]. The main advantage of a phase-blended free energy is that its convex hull can be straightforwardly identified through common-tangent constructions [55–57], simplifying equilibrium calculations and the derivation of conservation laws for the multiphase system.

In this Letter, we design a Gibbs free energy functional for methane-water mixtures under isobaric conditions that can be readily incorporated in phase-field models to study macroscopic interfacial processes. Our energy definition is thermodynamically consistent while numerically tractable, as it describes the phenomenological nonequilibrium dynamics of the hydrate system at macroscopic scale, while still predicting the correct thermodynamic equilibrium.

The equilibrium phase diagram is calculated through a simplified Gibbs free energy. In its minimal form, the system we study consists of three phases—methane-rich gas (V), methane-poor liquid (L_w), and hydrate (H)—and two components— CH_4 and H_2O . We denote by ϕ_α the volumetric fractions of phase α , where $\alpha = g, l, s$ refers to the vapor, liquid, and hydrate phase, respectively. At any given point in the domain they satisfy $\phi_g + \phi_l + \phi_s \equiv 1$. The system is also characterized by the pointwise methane mass fraction, $\chi = m_{\text{CH}_4}/(m_{\text{CH}_4} + m_{\text{H}_2\text{O}})$, or by the molar fraction, $C = n_{\text{CH}_4}/(n_{\text{CH}_4} + n_{\text{H}_2\text{O}})$. The two quantities are related by $\chi = M_{\text{CH}_4}C/[M_{\text{CH}_4}C + M_{\text{H}_2\text{O}}(1 - C)]$, where $M_{\text{CH}_4} = 16$ g/mol and $M_{\text{H}_2\text{O}} = 18$ g/mol are molar masses. Because the molar masses of the two components are similar, we can approximate $C \approx \chi$.

An isobaric phase diagram describes the equilibrium phase behavior of the system in temperature (T) and composition (χ) space at a fixed pressure; the T - χ phase diagram is discussed in detail in [5,6] and shown here in Fig. 1(b). We focus on phase behavior above the freezing point temperature, where pure water ice does not form [Fig. 1(b), red-boxed region]. This region exhibits four key features: (1) a boiling point temperature T^B , above which only vapor (V) exists; (2) a triple-point temperature T^T , where three phases coexist; (3) above T^T , a two-phase region of L_w - V coexistence; and (4) below T^T and above freezing, a hydrate-forming region (H) where either H - V or L - H equilibrium occurs.

For a given phase α at a fixed pressure, we formulate its corresponding Gibbs free energy, denoted f_α , as a function of χ and T . We use Wilson’s model for the liquid and gas phases [58], and a parabolic form for the solid phase [51,59,60],

$$f_l(\chi, T) = \omega_{\text{mix}} \{ \chi \log(\chi) - (1 - \chi) \log(1 - a_l(T)\chi) - \chi \log[1 - b_l(1 - \chi)] + f_{l0} \}, \quad (1)$$

$$f_g(\chi, T) = \omega_{\text{mix}} \{ \chi \log(\chi) - (1 - \chi) \log(1 - a_g\chi) - \chi \log[1 - b_g(T)(1 - \chi)] + f_{g0} \}, \quad (2)$$

$$f_s(\chi, T) = \omega_{\text{mix}} \{ a_s(T)(\chi - \chi_s)^2 + b_s(T) + f_{s0} \}, \quad (3)$$

where ω_{mix} (J/cm³) is a characteristic energy density. We account for nonlinear temperature dependence of f_α as suggested by [58] for gas and liquid [Eqs. (1)–(2)], and as suggested by the solidification literature [51,59,60] for the solid phase [Eq. (3)], $a_l = a_{l0}/(T/T_c)^4$, $b_g = b_{g0}/(T/T_c)^2$, $a_s = a_{s0}(T/T_c)$ and $b_s = b_{s0}(T/T_c)$, where $T_c = 1$ K is the scaling temperature.

For a given phase pair α and β , the equilibrium composition of each phase, $\chi_\alpha^{\alpha\beta}$ and $\chi_\beta^{\alpha\beta}$, is obtained through the common tangent construction [55–57], where we solve the system of two equations, $f'_\alpha(\chi_\alpha^{\alpha\beta}) = f'_\beta(\chi_\beta^{\alpha\beta})$ and $f_\alpha(\chi_\alpha^{\alpha\beta}) - f_\beta(\chi_\beta^{\alpha\beta}) = (\chi_\alpha^{\alpha\beta} - \chi_\beta^{\alpha\beta})f'_\alpha(\chi_\alpha^{\alpha\beta})$. In a three-phase system, the calculation is performed three times. Using the parameters given in Table I (for pressure $P = 5$ MPa), Fig. 2(a) illustrates free energy curves and their corresponding feasible tangent constructions at four different temperatures. At the triple-point temperature $T^T = 18.6$ °C, the dashed line is tangent to all three curves. Above T^T , at $T = 20, 60$ °C, hydrate does not form and gas-liquid equilibrium is favored, yielding two equilibrium compositions χ_l^{gl} and χ_g^{gl} . Below T^T , at $T = 5$ °C, hydrate can readily form and the equilibrium is defined by four composition values (from left to right), χ_l^{ls} , χ_s^{ls} , χ_s^{sg} , and χ_g^{sg} , which divide the χ axis into five different equilibrium scenarios [Fig. 2(f)].

Based on the calibrated parameters in Table I, here we calculate equilibrium compositions for a wide range of

TABLE I. Parameters used for Gibbs free energy calculations, with $a_g = 1$, $b_l = 1$, $f_{g0} = 20$, and $f_{l0} = -20$.

| P | b_{g0} | a_{l0} | a_{s0} | χ_s | b_{s0} | f_{s0} |
|--------|-----------------------|-----------------------|----------|----------|----------|----------|
| 5 MPa | -9.5×10^{10} | -9.5×10^{10} | 350 | 0.147 | 1.13 | -42 |
| 30 MPa | -1×10^9 | -1×10^9 | 1200 | 0.146 | 0.65 | -40 |

temperatures (increment of 0.1 K) and plot the results on a T - χ plane [Figs. 2(b)–2(e)]. At $P = 5$ MPa, the calculated phase diagram [Figs. 2(b) and 2(c)] agrees well with that obtained from experimental measurements and thermodynamic simulators in [5,6] [Fig. 1(b)]. Our results also correctly capture the triple-point $T^T = 280$ K and the boiling point $T^B = 537.15$ K. At $P = 30$ MPa, we focus our comparison with experiments on the hydrate-forming region, where χ is expected to be equal to 0.148, based on methane hydrate stoichiometry ($\text{CH}_4 \cdot 5.75\text{H}_2\text{O}$), but instead Raman spectroscopy measurements and thermodynamic simulators have demonstrated that nonstoichiometry methane concentrations are favored [5,6]. For instance, at $P = 30$ MPa and $T \approx 277$ K, $\chi_s^{sl} \approx 0.141$ and $\chi_s^{sg} \approx 0.1465$. In a T - χ phase diagram, such nonstoichiometry effects are evidenced by a separation between the L_w - H and H - V phase boundaries [Fig. 2(e)], which is well captured by our model [Fig. 2(d)]. In the context of hydrate growth on a gas-liquid interface, the nonstoichiometry effect indicates that hydrate that grows into a methane-rich gas phase may have higher methane concentration than hydrate that grows into a methane-poor liquid phase.

Nonequilibrium dynamics is studied using phase-field modeling. We define $\boldsymbol{\phi} = [\phi_g, \phi_l, \phi_s]$. Under the phase-field framework, the f_α 's are incorporated into the total free energy $F(\chi, \boldsymbol{\phi}, T)$, which also considers the energetic interactions between phases, and is composed of the bulk free energy f_0 and the interfacial energy (gradient squared terms),

$$\begin{aligned}
 F = \int_V [& f_0(\chi, \boldsymbol{\phi}, T) + \epsilon_c^2(T) |\nabla \chi|^2 \\
 & + \epsilon_{gl}^2(T) \nabla \phi_g \nabla \phi_l + \epsilon_{gs}^2(T) \nabla \phi_g \nabla \phi_s \\
 & + \epsilon_{sl}^2(T) \nabla \phi_s \nabla \phi_l + \epsilon_g^2(T) |\nabla \phi_g|^2 \\
 & + \epsilon_l^2(T) |\nabla \phi_l|^2 + \epsilon_s^2(T) |\nabla \phi_s|^2] dV. \quad (4)
 \end{aligned}$$

The bulk free energy, $f_0(\chi, \boldsymbol{\phi}, T)$, is made of two parts, $f_0 = \omega_{\text{mix}} \{G_g(\boldsymbol{\phi})f_g(\chi, T) + G_l(\boldsymbol{\phi})f_l(\chi, T) + G_s(\boldsymbol{\phi})f_s(\chi, T)\} + \omega_{gl}\phi_g^2\phi_l^2 + \omega_{gs}\phi_g^2\phi_s^2 + \omega_{sl}\phi_s^2\phi_l^2$. The blending functions $G_\alpha(\boldsymbol{\phi})$ for a three-phase system are taken from [61] as $G_\alpha(\boldsymbol{\phi}) = 0.25\phi_\alpha^2 \{15(1 - \phi_\alpha)[1 + \phi_\alpha - (\phi_\beta - \phi_\gamma)^2] + \phi_\alpha(9\phi_\alpha^2 - 5)\}$. The evolution of the system is driven by potentials Ψ (variational derivatives of F) and described by Cahn-Hilliard and Allen-Cahn-type equations,

$$\frac{\partial \chi}{\partial t} + \nabla \cdot (\mathbf{u}\chi) - R_\chi \nabla \cdot [D(\boldsymbol{\phi}) \nabla \Psi_\chi] = 0, \quad (5)$$

$$\frac{\partial \phi_\alpha}{\partial t} + \mathbf{u} \cdot \nabla \phi_\alpha + R_\phi \Psi_\alpha = 0, \quad \phi_l + \phi_g + \phi_s = 1, \quad (6)$$

where R_χ is an effective rate of diffusion (the inverse of a Péclet number) and R_ϕ is an effective rate of phase transition (the inverse of a capillary number) [46]. We assume simple hydrodynamics, with a Darcy-type mixture velocity, $\mathbf{u} = -[1/\mu(\boldsymbol{\phi})]\nabla p$, where p is a global fluid pressure obtained by imposing the incompressibility constraint, $\nabla \cdot \mathbf{u} = 0$, with appropriate boundary conditions. Here, $D(\boldsymbol{\phi}) = \phi_g D_g + \phi_l D_l + \phi_s D_s$ is a dimensionless mixture diffusion coefficient (where D_g , D_l , and D_s are normalized by a characteristic gas-phase diffusion coefficient D_{gas}), and $\mu(\boldsymbol{\phi})$ is a similarly defined dimensionless mixture viscosity. We adopt $D_g = 1$, $D_l = 10^{-3}$, and $D_s = 10^{-11}$ (whose relative magnitudes are consistent with

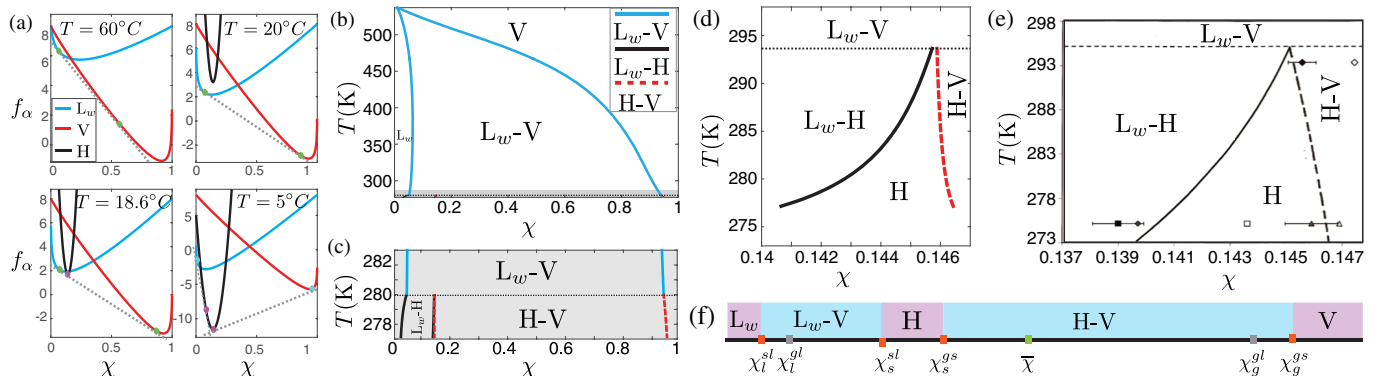


FIG. 2. (a) Gibbs free energy of all phases at various temperatures: green and red dots, equilibrium compositions; dashed grey lines, common tangents. At 5 MPa, (b) analytically calculated T - χ phase diagram; (c) enlarged version of the shaded grey area in (b); at 30 MPa, focusing on the hydrate-forming region, (d) analytically calculated T - χ phase diagram; (e) T - χ phase diagram from experiments adapted from [5]. The dashed line marks T^T in all figures. (f) The division of the χ axis into five phase regions by four equilibrium points (orange), not drawn to scale. The grey points correspond to gas-liquid equilibrium, which is not feasible under hydrate-forming scenarios.

Detailed and organized figure highlighting the main results

experimental measurements [62,63] and emulate slow diffusion in liquid and extremely slow diffusion within hydrate), and $\mu_g = 1$, $\mu_l = 5$, and $\mu_s = 500$.

Hydrate growth on a quiescent gas-liquid interface is investigated using the proposed model. Taking $\mathbf{u} = \mathbf{0}$, the system of four constrained partial differential equations in Eqs. (5) and (6) is discretized using finite elements and a monolithically coupled implicit time integration scheme. The simulations are performed on a one-dimensional domain ($x \in [0, 0.5]$) that is initially filled with 3/4 liquid, 1/4 gas, and no hydrate [Fig. 3(a)]. Based on parameters reported in Table I (5 MPa) and at $T = 278$ K, L_w - H equilibrium is characterized by $\chi_l^{ls} \approx 0.010$, $\chi_s^{ls} \approx 0.13$ and H - V equilibrium is characterized by $\chi_s^{gs} \approx 0.148$, $\chi_s^{gl} \approx 0.960$. In the absence of hydrate, the L - V equilibrium is characterized by $\chi_l^{gl} \approx 0.063$, $\chi_g^{gl} \approx 0.925$. Informed by these equilibrium compositions, we perform two sets of simulations to investigate how the initial liquid methane concentration (χ_l^0) influences the growth direction and kinetics of hydrate at the gas-liquid interface [25].

In the first simulation [Fig. 3(b)], the liquid phase is initially supersaturated in methane, where $\chi_l^0 \approx 0.08 > \chi_l^{gl}$; in the second simulation [Fig. 3(c)], the liquid phase is initially undersaturated in methane, where $\chi_l^0 \approx 0.005 < \chi_l^{gl}$. In both simulations, the gas phase is initialized with $\chi_g^0 = 0.93$, and the domain-averaged concentration is $\bar{\chi} = 0.25$ and 0.19 , respectively [Fig. 2(f), green dot]. This indicates that, at equilibrium, we should expect H - V coexistence in both simulations.

Our simulations demonstrate that the initial liquid methane concentration determines the direction of hydrate growth at a gas-liquid interface. When liquid is initially supersaturated, our model predicts that hydrate grows predominantly towards the liquid phase [Fig. 3(b)], in agreement with experimental observations [22]. When the liquid is initially undersaturated, the hydrate layer thickens into both the liquid and gas phases [Fig. 3(c)], consuming a significant amount of gas in order to sustain hydrate formation. In the context of hydrate formation around a methane gas bubble, these results could explain why some hydrate-armored bubbles buckle due to depletion of gas pressure inside the bubble as hydrate forms in undersaturated water [17,64], while some hydrate-coated bubbles can stay inflated when hydrate forms in supersaturated conditions [19].

By tracking the domain-averaged hydrate fraction $\langle \phi_s \rangle$ over time for both simulations [Fig. 3(d)], we observe that hydrate thickens at a decreasing growth rate that eventually becomes close to 0 [Figs. 3(e) and 3(f), black curve], which agrees well with experimental studies [22]. As a result of this hydrate-formation shutdown, the domain arrives at a quasisteady configuration of three-phase coexistence [Fig. 3(a), bottom], which is not predicted by equilibrium calculations [Fig. 2(f), green dot] that instead predict H - V coexistence at steady state. The nonequilibrium steady state has been understood as a diffusion-limited phenomenon, where the extremely slow diffusion within the hydrate phase can severely hinder the continued growth of hydrate into the liquid phase [22,29,54]. By comparing hydrate growth rate against gas consumption rate [Figs. 3(e) and 3(f)] and analyzing details of composition profiles, here, we provide mechanistic insights into two distinct stages of this diffusion-limited growth. In the first stage [purple in Figs. 3(e) and 3(f)], gas is consumed to supply the methane needed for hydrate formation. During this stage, the liquid methane concentration, χ_l , remains constant if it is initially supersaturated, or increases if initially undersaturated. The hydrate phase methane concentration, χ_s , equals χ_s^{gs} (the H - V equilibrium). In the second stage, after a significant amount of hydrate has formed in between the gas and liquid, the gas-hydrate interface reaches equilibrium and hydrate growth stops on the gas side but continues into the liquid; no more gas is consumed [green in Figs. 3(e) and 3(f)]. During this stage, χ_l decreases towards χ_l^{ls} and χ_s also decreases towards χ_s^{sl} on the side that grows into the liquid. This second-stage growth is driven by the thermodynamically imposed compositional gradient within the hydrate phase [5], and is therefore limited by the extremely slow diffusion within the hydrate.

Persistent gas conduits in hydrate-bearing sediments have been widely observed in field surveys [7–9], although their formation mechanisms are not well understood. Here, we demonstrate that nonequilibrium hydrate growth on moving gas-liquid interfaces provides a plausible

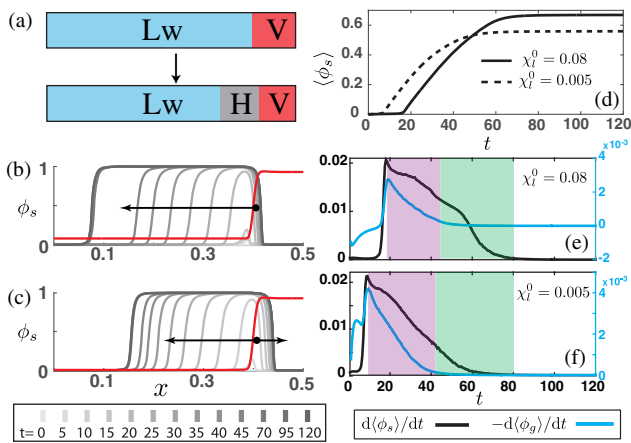


FIG. 3. (a) Schematic illustrating hydrate growth on a liquid-gas interface. Simulated profiles of ϕ_s at different times (grey scale) and initial profile of χ (red) for (b) initially supersaturated liquid and (c) initially undersaturated liquid. The black arrow points to growth direction and the black dot marks the position of initial gas-liquid interface. (d) Domain-integrated ϕ_s over time. [(e) and (f)] Domain-integrated hydrate growth rate (black) and gas consumption rate (blue) as a function of time, with gas-sustained (purple) and liquid-sustained (green) stages of hydrate growth.

The figures use clear labeling and color coding for organization

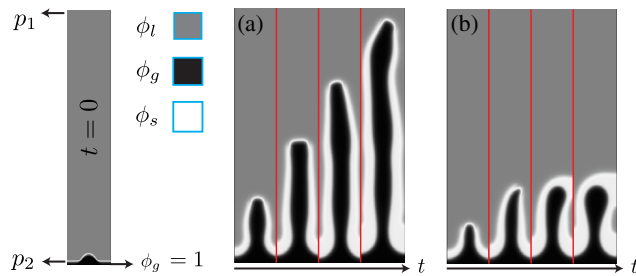


FIG. 4. Simulations illustrating hydrate-encased gas conduits forming in initially undersaturated liquid ($\chi_l^0 = 0.005 < \chi_l^s$). Simulation (a) corresponds to a pressure difference driving the flow that is twice that of simulation (b).

explanation for the formation of these gas conduits. We solve Eqs. (5) and (6) in a rectangular domain, with upward flow sustained by an imposed pressure gradient ($p_2 > p_1$), emulating buoyancy-driven gas migration in seafloor sediments (Fig. 4). We describe hydrate as a highly viscous fluid (viscosity contrast $\mu_s/\mu_g = 500$) that exerts significant resistance to the gas movement upon formation at the gas-liquid interface.

We show two simulations, where the only difference is the magnitude of the imposed pressure difference, $\Delta p = p_2 - p_1$: the pressure difference in the first simulation is twice that of the second simulation. In the first simulation [Fig. 4(a)], upward gas movement is fast enough to overcome the restraint of the hydrate layer, leading to continued elongation of the gas conduit. In the second simulation [Fig. 4(b)], gas moves relatively slowly, and the elongation of the gas conduit is hindered and eventually arrested by hydrate formation at the interface. The conduit becomes sealed off at the top, and the shape persists due to the extremely slow diffusion within the hydrate phase, leading to a long-lived nonequilibrium configuration.

In summary, we develop a continuum-scale phase-field model to study methane hydrate systems far from thermodynamic equilibrium. We design the bulk Gibbs free energy to describe thermodynamic equilibrium, which recovers the isobaric temperature-composition phase diagram from experimental studies. We then incorporate this free energy into a phase-field model to study formation dynamics of hydrate on a gas-liquid interface. Our model predicts that initial aqueous concentration exerts powerful control on the growth direction of hydrate, where hydrate grows dominantly into liquid if liquid is initially at/over saturation, and grows into both liquid and gas if liquid is initially undersaturated. This result has significant implications to the long-standing puzzle of why some hydrate-coated gas bubbles collapse due to hydrate formation [17,64] and some do not [19]. Our model correctly recovers the diffusion-limited kinetics of hydrate growth as measured in experiments. By tracking the source of methane supply during hydrate formation, we further demonstrate that hydrate growth is in fact two staged; in the first stage,

methane needed for hydrate formation is dominantly supplied from the gas phase; in the second stage, hydrate growth continues into the liquid phase without consuming any gas. This could explain the occurrence of persistent gas conduits in some hydrate-bearing sediments [7–9] and other nonequilibrium phenomena commonly observed in natural methane hydrate systems.

We thank Carolyn Ruppel and William Waite from USGS for insightful discussions. This work was funded in part by the U.S. Department of Energy (Awards No. DE-FE0013999 and No. DE-SC0018357). L. C. F. acknowledges funding from the Spanish Ministry of Economy and Competitiveness (Grants No. RYC-2012-11704 and No. CTM2014-54312-P). L. C. F. and R. J. acknowledge funding from the MIT International Science and Technology Initiatives, through a Seed Fund grant.

*juanes@mit.edu

- [1] E. D. Sloan, *Nature (London)* **426**, 353 (2003).
- [2] E. D. Sloan and C. A. Koh, *Clathrate Hydrates of Natural Gases*, 3rd ed. (CRC Press, Boca Raton, 2008).
- [3] A. L. Ballard and E. D. Sloan, *Fluid Phase Equilib.* **218**, 15 (2004).
- [4] A. L. Ballard and E. D. Sloan, *Fluid Phase Equilib.* **216**, 257 (2004).
- [5] Z. Huo, K. Hester, E. D. Sloan, and K. T. Miller, *AIChE J.* **49**, 1300 (2003).
- [6] E. D. Sloan, C. A. Koh, and A. K. Sum, *Energiespectrum* **3**, 1991 (2010).
- [7] E. Suess, M. E. Torres, G. Bohrmann, R. W. Collier, J. Greinert, P. Linke, G. Rehder, A. Trehu, K. Wallmann, G. Winckler, and E. Zuleger, *Earth Planet. Sci. Lett.* **170**, 1 (1999).
- [8] X. Liu and P. B. Flemings, *Earth Planet. Sci. Lett.* **241**, 211 (2006).
- [9] N. L. B. Bangs, M. J. Hornbach, and C. Berndt, *Earth Planet. Sci. Lett.* **310**, 105 (2011).
- [10] D. R. Topham, *Chem. Eng. Sci.* **39**, 821 (1984).
- [11] G. Rehder, P. W. Brewer, E. T. Peltzer, and G. Friederich, *Geophys. Res. Lett.* **29**, 21-1 (2002).
- [12] E. J. Sauter, S. I. Muyakshin, J.-L. Charlou, M. Schlüter, A. Boetius, K. Jerosch, E. Damm, J.-P. Foucher, and M. Klages, *Earth Planet. Sci. Lett.* **243**, 354 (2006).
- [13] G. Rehder, I. Leifer, P. G. Brewer, G. Friederich, and E. T. Peltzer, *Mar. Chem.* **114**, 19 (2009).
- [14] C. A. Graves, L. Steinle, G. Rehder, H. Niemann, D. P. Connelly, D. Lowry, R. E. Fisher, A. W. Stott, H. Sahling, and R. H. James, *J. Geophys. Res. Oceans* **120**, 6185 (2015).
- [15] B. Wang, S. A. Socolofsky, J. A. Breier, and J. S. Seewald, *J. Geophys. Res. Oceans* **121**, 2203 (2016).
- [16] B. B. Maini and P. R. Bishnoi, *Chem. Eng. Sci.* **36**, 183 (1981).
- [17] L. Chen, J. S. Levine, M. Gilmer, E. D. Sloan, C. A. Koh, and A. K. Sum, *J. Chem. Eng. Data* **59**, 1045 (2014).
- [18] L. Chen, J. S. Levine, M. Gilmer, E. D. Sloan, C. A. Koh, and A. K. Sum, *J. Chem. Eng. Data* **61**, 2647 (2016).

The main point is summarized immediately in the conclusion